3446 *Macromolecules* **2010**, *43*, 3446–3454
DOI: 10.1021/ma902332h

Macromolecules
ARTICLE

Interpolation in the Directed Assembly of Block Copolymers on Nanopatterned Substrates: Simulation and Experiments

François A. Detcheverry,[†] Guoliang Liu,[†] Paul F. Nealey, and Juan J. de Pablo*

Department of Chemical and Biological Engineering, University of Wisconsin, Madison, Wisconsin 53706.
[†]These authors contributed equally to this work.

Received October 22, 2009; Revised Manuscript Received February 18, 2010

ABSTRACT: A combined theoretical and experimental approach is used to study the directed assembly of a lamellae-forming block copolymer on chemically patterned substrates. The period of the pattern is lower than that of the copolymer, whose characteristic morphology is then used to interpolate the features of the substrate. The pattern considered in this study consists of stripes of width W repeated over the background substrate with period $L_P = 2L_0$, where L_0 is the copolymer natural period. The stripe and background areas are characterized by their affinities Λ_s and Λ_b for the blocks of the polymer. Using theoretically informed Monte Carlo simulations of a coarse-grained model, we investigate in a systematic manner the influence of the pattern parameters W, Λ_s, and Λ_b on the morphology of copolymer thin films. Thermodynamic integration is used to compute the free energy difference and the relative stability of competing morphologies. It is found that the parameter space considered here is dominated by nonbulk and often metastable morphologies. The conditions that yield successful interpolation of lamellae are identified. Consistent with theoretical predictions, experiments on patterned substrates with carefully controlled interfacial characteristics reveal new, three-dimensional morphologies that do not arise in the bulk. The sought-after vertical lamellae, which are desirable for pattern interpolation and lithography, are found to occur only when the interaction between one of the blocks and the background area is relatively weak.

I. Introduction

Understanding the self-assembled structures that arise when block copolymer thin films are deposited and equilibrated in the presence of chemically nanopatterned surfaces is of both fundamental and technological importance. Several key concepts emerge that are simply absent in the case of bulk materials. First, in the case of thin films, surface and interfacial energies play an important or even dominant role in the resulting morphology. If one averages surface and interfacial energy over the volume of the film and expresses the energy on a per-chain basis, the resulting values can exceed the block−block interfacial energy and the polymer configurational entropy that are used to explain the formation of spheres, cylinders, and lamellae in the bulk. Second, chemical patterns of defined interfacial interactions and controlled geometry allow for directed assembly of novel and as yet unknown nanostructures. Third, approaches that view the system as a bulk morphology "perturbed" by the substrate are of limited use; it is important to realize that the copolymer and the surface, together, constitute a new system whose behavior remains largely unknown.

Three distinct regimes can be identified: (1) the patterned features have dimensions L_P much larger than the characteristic period of the block copolymer L_0 ($L_P \gg L_0$), (2) the spacing between features is only a few times larger than the block copolymer period ($L_P \approx (2-5)L_0$), and (3) the features and block copolymers have similar dimensions ($L_P \approx L_0$). In each regime, the strength of interfacial energy between the features of the chemical pattern and the blocks of the copolymers may be varied from strong to weak to neutral, and the geometry of the pattern may or may not be matched in symmetry to the bulk morphology of the copolymer. In this vast parameter space, only a small number of block copolymer materials and cases have been considered, and development of molecular modeling tools to explore this space is essential.

The experimental system that has been explored most extensively so far is poly(styrene-*block*-methyl methacrylate) or P(S-*b*-MMA). An unusual characteristic of this material is that the surface energy of the two blocks is nearly equal at the temperature of assembly (annealing), which serves to accentuate the impact of interfacial interactions with the chemical patterns and to diminish the role of surface energy which could otherwise dominate the system behavior. From a technological standpoint, this system is also interesting because the PMMA block may be removed, and materials have been developed to pattern and quantitatively control interfacial interactions.

In regime 1, a symmetric block polymer tends to form lamellae oriented parallel to the substrate, with symmetric or asymmetric wetting (the film thickness is nL_0 or $(n + 1/2)L_0$, respectively, where n is an integer). On patterns that induce alternating symmetric and asymmetric wetting over regions of size L_P, strong interfacial energies combined with large L_P lead to a fast ordering and allow for cooperative assembly across adjacent regions, even over dimensions of tens of micrometers.[1] As the dimensions of the patterned regions shrink, the quantization in film thickness on adjacent regions begins to break down, around $L_P \approx 30L_0$.[2]

In regime 3, an exquisite degree of control over the morphology of the block copolymer film can be realized. In one major application area, the integration of self-assembling block copolymers with traditional lithographic techniques can advance and augment patterning performance considerably. We and others have demonstrated that directed assembly of copolymers enables fabrication at length scales not possible with current

*To whom correspondence should be addressed.

 Published on Web 03/05/2010

materials and processes, that it retains the essential attributes of existing manufacturing practices, including perfection, registration, and the ability to pattern complex device-oriented architectures, and that it may offer sub-1 nm dimensional control and line-edge roughness. In a second area of interest, it has been shown that by equilibrating a block copolymer in the presence of a chemical pattern (a pattern that does not replicate the geometry of the block copolymer morphology in the bulk), one can achieve three-dimensional ordering from two-dimensional patterns, with the formation of a new bicontinuous morphology.[3]

Investigations related to regime 2 have been scarce. One aim of studies pertaining to regime 2 that does not apply to regimes 1 and 3 is to understand the interpolation of assembled structures in the block copolymer film between features of the underlying chemical pattern. Park et al., for example, directed the assembly of a cylinder-forming P(S-*b*-MMA) on chemically nanopatterned surfaces consisting of a square array of spots with varying lattice spacing and spot size.[4] Under certain conditions, domains were formed, i.e., interpolated, in the center of the square unit cells defined by the chemical pattern. Using patterns with geometries matching the those of the overlying block copolymer, cylinder-like and lamellae-like morphologies have been interpolated.[5−7] This interpolation technique may have considerable technological importance, for example, in applications related to patterned storage media.

In this work we aim to develop a fundamental understanding of interpolated morphologies of lamellae-forming block copolymers on chemically striped surfaces through a combination of theory and experiments. More specifically, we seek to address three questions: (i) What kind of morphologies, nonbulk in particular, arise on incomplete patterns? (ii) What are the optimal conditions for successful interpolation? (iii) How tolerant is the interpolation process with respect to the pattern properties? We focus on a lamellae-forming block copolymer with period L_0, laid over a striped pattern whose period is twice that of the polymer ($L_P = 2L_0$). The stripe width W and pattern affinities are varied in a systematic manner. Using simulations, possible morphologies are determined from a combinatorial exploration of this parameter space. We then show how thermodynamic integration can be used to extract phase boundaries between competing morphologies. On the experimental front, we use e-beam and interferometric lithography to create surface patterns with varying dimensions. Thin copolymer films of P(S-*b*-MMA) are then spin-coated and annealed, and the resulting morphologies are characterized by scanning electron microscopy (SEM).

Our article begins with a discussion of the model and computational methods that are employed to describe copolymer films, followed by a description of the experimental system and procedures. We then present extensive simulations carried out over a wide range of parameter space. Those results are discussed and interpreted in the context of experimental data gathered for conditions that closely resemble those considered computationally. We conclude with a few remarks pertaining to the overall robustness of the proposed interpolation strategy.

II. Methods

Model and Parameters. Our simulations rely on a traditional coarse-grained model for block copolymer melts[8] that incorporates three main ingredients: the chain connectivity, the repulsion between unlike monomers, and the finite compressibility of the melt. Chains are Gaussian and discretized into N beads, with the position of the sth bead in the lth chain denoted by $\mathbf{r}_l(s)$. For a number n of AB copolymer

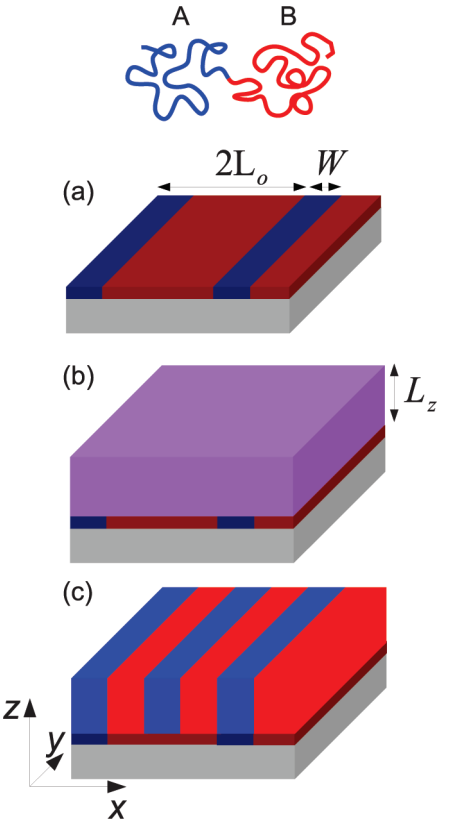

Figure 1. Schematic representation of the copolymer film on a substrate patterned with stripes of width W and period $L_P = 2L_0$ (a). A thin film of a symmetric block copolymer is annealed on the substrate (b) and allowed to self-assemble (c).

molecules in a volume V at temperature T, the Hamiltonian is given by

$$\frac{\mathscr{H}}{k_B T} = \frac{3}{2}\sum_{l=1}^{n}\sum_{s=1}^{N-1}\frac{N-1}{{R_e}^2}\left[\mathbf{r}_l(s+1)-\mathbf{r}_l(s)\right]^2 + \sqrt{\bar{N}}\int_V \frac{\mathrm{d}\mathbf{r}}{{R_e}^3}\left[\chi N\phi_A\phi_B + \frac{\kappa N}{2}\left(1-\phi_A-\phi_B\right)^2\right] \quad (1)$$

Here, k_B is the Boltzmann constant, ${R_e}^2$ is the mean-squared end-to-end distance for an ideal chain, and $\sqrt{\bar{N}} = \rho_0 {R_e}^3/N$ is the interdigitation number. The quantity ρ_0 denotes the bead density. The local densities $\phi_{K=A,B}$ are computed from the bead positions by counting the number of beads in the cells of a regular grid with spacing ΔL. To model the thin film considered in experiments, chains are confined between two hard walls. The top surface is neutral, whereas the effect of the patterned substrate is represented with a potential U_S acting on each bead

$$\frac{U_S(\mathbf{r},K)}{k_B T} = -\frac{\Lambda_S^K}{d_S/R_e}\exp\left[-\frac{z^2}{2{d_S}^2}\right] \quad (2)$$

where $\Lambda_S^K N$ determines the strength of interaction between beads of type K and the pattern substrate S. The self-assembled morphologies are determined from Monte Carlo (MC) simulations. Additional details about the model and methods are given in ref 9.

We consider a symmetric diblock for which $\chi N = 25$, $\kappa N = 35$, and $\bar{N} = 110$;[19] these parameters correspond to a P(S-*b*-MMA) diblock with molecular weight around 74 kg

mol^{-1}. The chain discretization is set to $N = 32$ and the grid spacing to $\Delta L = 0.166R_e$. The natural repeat period is $L_0 = 1.66R_e$. As shown in Figure 1, the pattern consists of stripes of width W repeated with a period $L_P = 2L_0$. Unpatterned regions are referred to as the "background". The interactions between the two blocks (A or B) and the two patterned areas (stripe or background) are specified by the four parameters $\Lambda_b^A N$, $\Lambda_s^A N$, $\Lambda_b^B N$, and $\Lambda_s^B N$. To reduce the parameter space, we assume that for both patterned areas the repulsion for the nonpreferred block is equal in magnitude to the attraction for the preferred block, that is, $-\Lambda_s^B N = \Lambda_s^A N = \Lambda_s$ and $-\Lambda_b^A N = \Lambda_b^B N = \Lambda_b$. In the following, Λ_s and Λ_b are referred to as the stripe and background affinities, respectively. In experiments, for a given diblock, Λ_b is controlled by the brush covering the substrate, while W and Λ_s depend on the mask and the exposure.

Experiment. A chemical pattern modified from a polystyrene (PS) imaging layer was used in experiments to direct the self-assembly of block copolymers. A 5 nm film of hydroxyl-terminated polystyrene (PS−OH, 6 kg mol^{-1}) was anchored to a silicon wafer with a thin layer of native oxide by spin-coating a 1.0 wt % PS−OH solution in toluene, followed by baking at 160 °C under vacuum for one day. Excess polymer was washed away with toluene. The resulting PS image layer was dried under a nitrogen stream and then covered by a 50 nm film of photoresist (PMMA, 960 kg mol^{-1}). The PMMA was patterned using EUV-XIL ($\lambda = 13.4$ nm) or electron beam lithography to yield a grating with period $L_P = 90$ nm. The width of the exposed lines was varied by tuning the dosage of X-ray or electrons delivered to the substrate. After exposure, the PMMA was developed in a mixture of methyl isobutyl ketone (MIBK) and isopropanol (IPA) (volume ratio = 1:3) for 40 s and then rinsed with IPA before drying under a nitrogen stream. The PMMA gratings were imaged using a LEO 1550 VP field emission scanning electron microscope. The topographic PMMA pattern after development was subject to oxygen plasma to form a chemical pattern of alternating PS stripes and oxidized PS stripes in the protected and unprotected areas, respectively. The remaining photoresist was stripped off by sonicating in warm chlorobenzene, over a period of 3 min, three times. A symmetric P(S-*b*-MMA) diblock copolymer (M_w = 37−37 kg mol^{-1} and $L_0 = 45$ nm) was deposited on the patterned substrate by spin-coating from a dilute solution in toluene, with a film thickness $L_z = L_0$. The systems were annealed at 230 °C for three days, and the resulting block copolymer morphologies were imaged with SEM.

III. Results

A. Exploration of Parameter Space. We seek to identify all the morphologies that can arise on the pattern described above. Although the film thickness is one of the key parameters controlling the type of morphologies, here it is fixed to the experimental value $L_z = L_0$. We focus on the influence of the three pattern parameters: four stripe widths are considered (W/L_0 = 0.25, 0.5, 0.75, and 1), and for a relatively short-range potential ($d_S = 0.15R_e$), the pattern affinities Λ_b and Λ_s are varied from 0 to 2. Such range is consistent with the order of magnitude estimate given in a previous study.[10] Since the pattern area is completely covered by its preferred block for the maximal value $\Lambda = 2$, stronger affinities are not expected to result in new morphologies.[20] The simulation box has dimensions $L_x \times L_y \times L_z$, with $L_x = 4L_0$ and $L_y = 4L_0$ or $8L_0$. A variety of MC moves are necessary to efficiently equilibrate the system: in addition to the displacement of a single bead, we use reptation, whole-chain translations, and swapping of the two blocks. The soft nature of the interaction between beads ensures that such global moves have a significant acceptance probability. Even though the final morphologies are usually reached relatively early in a calculation, all simulations were run for at least 10^5 MC steps.[21]

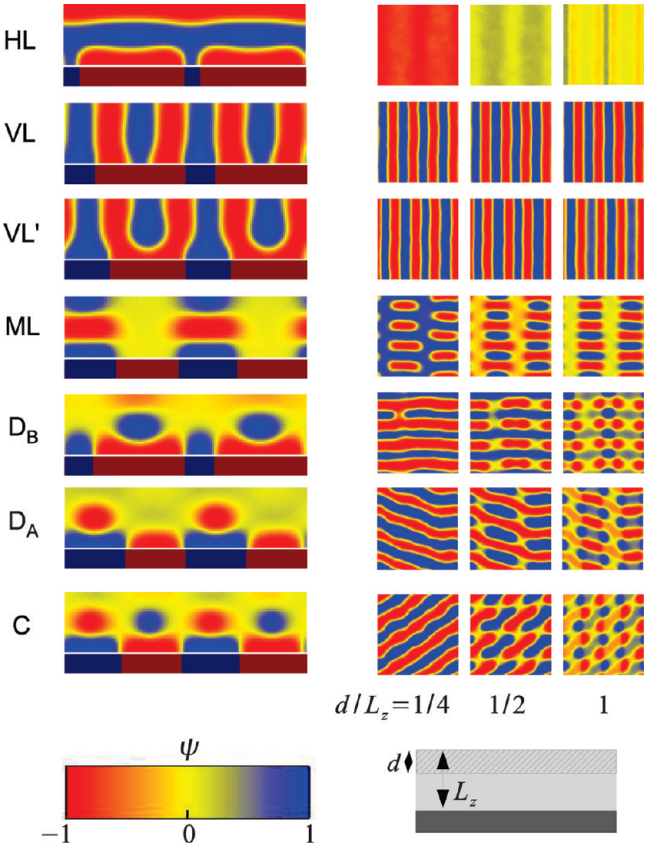

Figure 2. Morphologies observed in simulations: horizontal lamellae (HL), vertical lamellae without or with asymmetry (VL or VL′), mixed lamellae (ML), A and B dots (D_A and D_B), and checkerboard (C). Each color map shows the local composition: $\psi = \langle(\phi_A - \phi_B)/(\phi_A + \phi_B)\rangle$. (left) Average composition in the $x-z$ plane. The (x, y, z) axes are defined in Figure 1, and the pattern is shown schematically below the color maps. (right) Average composition in the $x-y$ plane, computed in a layer of depth d with d/L_z = 1/4, 1/2, and 1. The scale is different in the two columns.

Within the parameter space explored in this work, simulations indicate that five distinct morphologies should be observed; they are shown in Figure 2. While all morphologies are fully three-dimensional, two-dimensional color maps are sufficient to discriminate between them. An "$x-z$ color map" plots the average local composition in the $x-z$ plane; i.e., an average over the y direction is taken. Also shown are "$x-y$ color maps" (which, for brevity, we refer to as "color maps" in what follows). We also present the average composition computed in an uppermost layer of depth $d = L_z/4$ or $L_z/2$. This is useful to better describe the morphology and to make contact with experimental micrographs obtained by SEM. Three morphologies retain the lamellar character of the bulk system: the horizontal, vertical, and mixed lamellae morphologies. They differ in the local orientation of the domains. In mixed lamellae, the domains are horizontal above the stripe and vertical above the background. Vertical lamellae are of two types: the two B domains laying on the background are either disjointed or connected by a thin layer covering the substrate. The latter feature arises when the background affinity is sufficiently strong and results in the

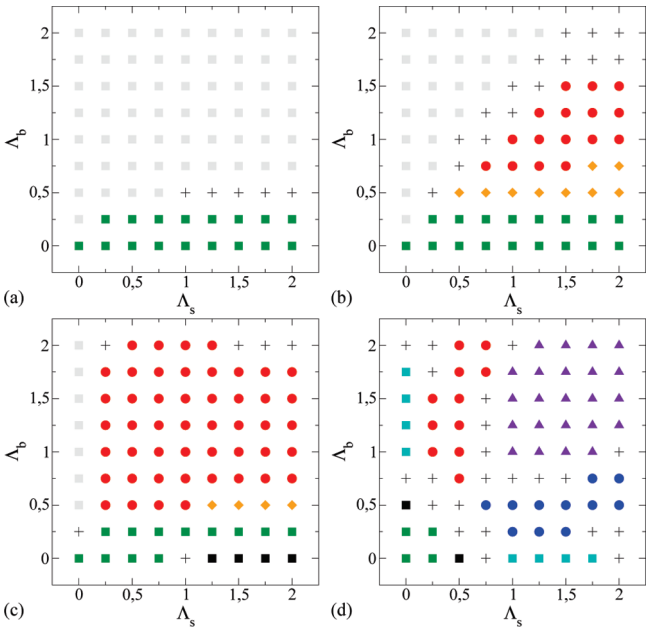

Figure 3. Morphologies observed as a function of the stripe affinity Λ_s and background affinity Λ_b. From (a) to (d), the stripe widths are W/L_0 = 0.25, 0.5, 0.75, and 1. A correspondence to the morphologies described in Figure 2 is provided by the symbol color and shape: horizontal lamellae (gray squares), vertical lamellae (green squares), mixed lamellae (black squares), checkerboard (purple triangles), B dots (red dots), and A dots (blue dots). "Hybrid" structures are included in the figure: dots and vertical lamellae (orange diamonds), horizontal and mixed lamellae (light blue squares). Cases where the morphology could not be assigned unequivocally are denoted with a plus sign.

two A domains having different dimensions and shapes, an asymmetry that is visible in the $x-y$ color maps. In the checkerboard morphology, the lower part of the film replicates the pattern, and the domains above replicate its opposite. The uppermost layer exhibits lamellar domains with period comparable to L_0 and whose orientation is not dictated by the underlying pattern. A similar feature is observed for the dot morphology. In the B dots, the B domains form "bridges" that straddle the A domain covering each stripe. Such structures appear in the $x-y$ color map as periodically arranged pairs of dots, with one dot on each side of the stripe.

Overview. To investigate the influence of pattern properties W, Λ_b, and Λ_s, more than 300 combinations of parameters were considered; up to five simulations were carried out in each case. Figure 3 reports the morphology that is predominantly obtained at any given point. When two morphologies are consistently observed—either in distinct realizations or in different regions of the same simulation box—this is indicated in the figure. In some cases, the morphology could not be assigned unequivocally.

The stripe width has considerable influence on the observed set of morphologies. For the thinnest stripes (W/L_0 = 0.25), horizontal lamellae are predominant. This can be expected since the film thickness is equal to the natural block copolymer period ($L_z = L_0$), and the background, which occupies most of the substrate area, favors the parallel orientation as soon as $\Lambda_b > 0$. As a result, only the lowest background affinities yield vertical lamellae. Increasing the stripe width to W/L_0 = 0.5 leads to the appearance of the dot morphology. Between areas of lamellae and dots, "hybrid" structures that include both morphologies are consistently obtained. The case of large

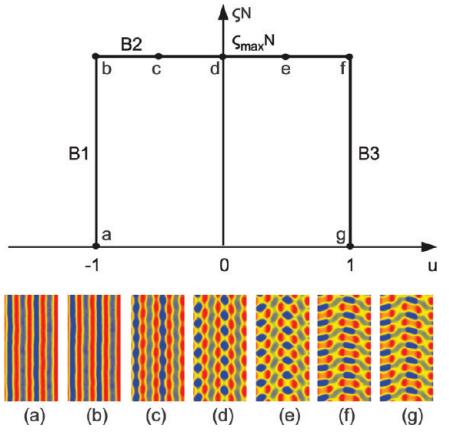

Figure 4. Thermodynamic integration path connecting the lamellar and dot morphologies; ζN is the strength of the external field, and u is a mixing parameter. B1 and B3 denote the "field" branches, and B2 denotes the "mixing" branch. Color maps (a–g) show the gradual transition from one morphology to another.

stripes (W/L_0 = 0.75) is dominated by the dot morphology, which is seen in 48 out of 81 state points. Finally, a symmetric pattern with $W = L_0$ can lead to six distinct morphologies, including the checkerboard. It is apparent from Figure 3 that vertical lamellae arise only over a small portion of the parameter space explored here. The most important condition for such successful interpolation is that the background attracts only weakly its preferred block, i.e., a rather low Λ_b (≈0.25). When this condition holds, the interpolation process is relatively robust: vertical lamellae arise over a large range of stripe widths ($0.25 \leqslant W/L_0 \leqslant 0.75$ at least) and for almost all stripe affinities considered here ($0.25 \leqslant \Lambda_s \leqslant 2$).

B. Thermodynamic Integration and Metastability. A combinatorial exploration of the parameter space gives the set of morphologies that can be expected and a qualitative idea of the phase diagram. However, as explained above, MC simulations sometimes yield "hybrid" structures, and it becomes difficult to identify the equilibrium morphology. To delineate phase boundaries, it is necessary to determine the free energy of each phase. In this section, we show how to compute the free energy difference between morphologies using thermodynamic integration. For clarity, the method is illustrated by considering the competition between dots and vertical lamellae. The former is the most common morphology, and the latter is arguably the most useful in applications. We choose a stripe width W/L_0 = 0.75 because wider stripes are generally easier to pattern experimentally. It is also interesting to see whether the self-assembled copolymer can correct this significant mismatch with the natural domain dimension; note that such a large rectification effect has only been demonstrated in the context of interpolation with cylinders.[5]

Integration Path and External Field. The free energy change in going from a thermodynamic state α to a state β upon changing a parameter u is given by

$$\Delta F_{\alpha\to\beta} = \int_{u_\alpha}^{u_\beta} \mathrm{d}u \left\langle \frac{\partial \mathscr{H}}{\partial u} \right\rangle \qquad (3)$$

where $\langle\,\rangle$ denotes a thermodynamic average. The intermediate states between α and β are assumed to form a path that is continuous and reversible. To define such a path, we introduce a three-dimensional "external field" that prevents any abrupt transition by maintaining the system in a predefined

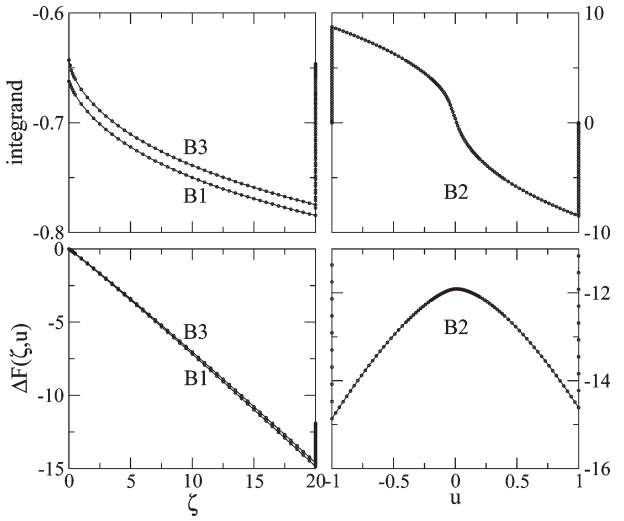

Figure 5. Integrand for the integrals of eq 5 and free energy difference ΔF along the integration path as a function of the external field strength ζ and the mixing parameter u. Branches B1, B2, and B3 are defined in Figure 4.

morphology. Similar to the pattern field, this external field is defined as

$$\frac{U_{\text{ext}}(\mathbf{r}, K)}{k_{\text{B}}T} = -\zeta f_{\text{ext}}(\mathbf{r}, K) \tag{4}$$

where ζN determines the strength of the field and f_{ext}, of order 1 in magnitude, describes its spatial variations. The Hamiltonian then includes the additional term $\mathscr{H}_{\text{ext}} = \sum_i U_{\text{ext}}(\mathbf{r}_i, K_i)$, where the sum runs over all beads i. For a given morphology α, a corresponding external field $f^{\alpha}_{\text{ext}}(\mathbf{r})$ can be defined from the local densities; one possible choice is $f^{\alpha}_{\text{ext}} = \langle(\phi_{\text{A}} - \phi_{\text{B}})/(\phi_{\text{A}} + \phi_{\text{B}})\rangle$. As illustrated in Figure 4 for the case of lamellae and dots, the integration path includes three branches. Starting from the α morphology, the corresponding external field f^{α}_{ext} is applied, with a strength that is increased up to its maximal value $\zeta_{\max}N$. Then, using the interpolated field $f_{\text{ext}} = {}^1/_2[(1-u)f^{\alpha}_{\text{ext}} + (1+u)f^{\beta}_{\text{ext}}]$, where the mixing parameter u goes from -1 to 1, the α morphology is gradually converted into the β morphology. Finally, the external field is turned down to zero. Note that in Figure 4 the thermodynamic parameters are the same at both ends of the path, since one end corresponds to a metastable state. Consequently, the thermodynamic average of eq 3 is not performed over all possible configurations but is restricted to configurations compatible with one morphology (α or β). The free energy change along the "external field" path is given by

$$\Delta F_{\alpha\to\beta} = \int_0^{\zeta_{\max}N} \mathrm{d}\zeta N \frac{\langle \mathscr{H}^{\alpha}_{\text{ext}} \rangle}{\zeta N} + \int_{-1}^{1} \frac{\mathrm{d}u}{2} \langle -\mathscr{H}^{\alpha}_{\text{ext}} + \mathscr{H}^{\beta}_{\text{ext}} \rangle + \int_{\zeta_{\max}N}^{0} \mathrm{d}\zeta N \frac{\langle \mathscr{H}^{\beta}_{\text{ext}} \rangle}{\zeta N} \tag{5}$$

The thermodynamic integration scheme employed here is similar to that presented in ref 11, where thermodynamic integration was used to locate the order−disorder transition of a symmetric diblock copolymer. Our implementation differs in two respects: (i) the external field couples to the position of beads rather than to the local densities, and (ii) the path connects an equilibrium to a metastable morphology, instead of two equilibrium states.

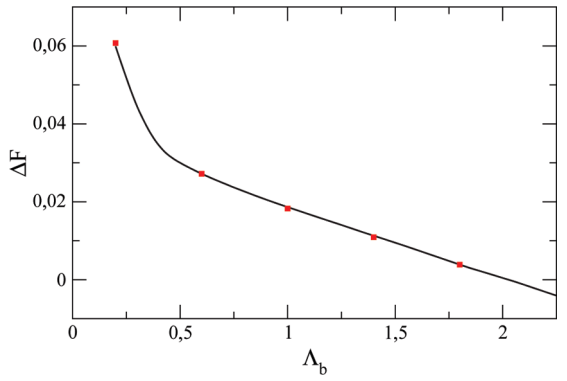

Figure 6. Free energy difference between dots and lamellae as a function of the background affinity Λ_{b}. Here $\Lambda_{\text{s}} = 1$. ΔF was computed in two ways: either by thermodynamic integration along the external field path for $\Lambda_{\text{b}} = 0.2$, 0.6, 1, 1.4, and 1.8 (points) or by simple thermodynamic integration along Λ_{b}, taking $\Lambda_{\text{b}} = 0.6$ as the reference point (line).

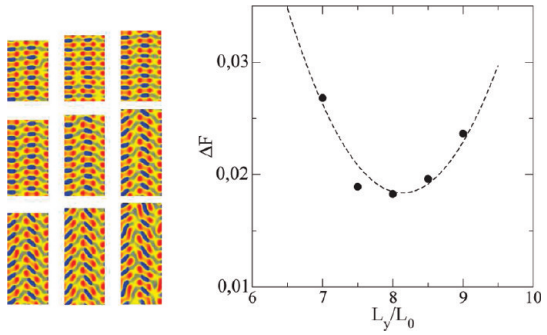

Figure 7. Properties of dots upon changing the period d_y imposed by the box width L_y. (left) Color maps for L_y/L_0 varying from 6.5 to 10 with 0.5 increments. (right) Free energy difference between dots and lamellae as a function of period L_y/L_0. The line is a parabolic fit to the data.

Computation of ΔF. The free energy difference between the dot and lamellar phases, expressed in units of $k_{\text{B}}T$ per chain, is denoted by $\Delta F = F_{\text{dot}} - F_{\text{lam}}$. Figure 5 plots the integrand and free energy difference along each branch of the external field path, which has been discretized into approximately 200 points. While the integrand is always continuous along the field branches B1 and B3, a discontinuity can be observed along the mixing branch B2 when the external field is not sufficiently strong. If, for instance, $\zeta_{\max}N = 1$, the lamellae and dot morphologies (albeit deformed by the field) are both stable, and the system abruptly shifts from one morphology to the other. Choosing $\zeta_{\max}N = 20$ as in Figure 5 ensures that there is only a single possible state along B2 and no discontinuity. Compared to the maximum of $\Delta F(\zeta,u)$ reached along the path, the final value ΔF is considerably smaller (by a factor 10^3) because it results from almost canceling contributions, either from points of equal ζN on branches B1 and B3 or from points with mixing parameters $\pm u$ on branch B2. The large difference between the maximal and final ΔF could cast some doubts on the accuracy of the method. In practice, however, simulations with strong external fields equilibrate rapidly, and accurate averages can be obtained. Furthermore, we have verified that computing ΔF along two independent paths gives consistent results (see Figure 6).

Finite-Size Effects on the Dot Morphology. Since the size of the simulation box is kept constant in this work (see ref 12 for a different approach), it is important to verify that finite-size effects are negligible. The dot morphology is periodic along the y direction; we denote by D_y its natural period and by d_y

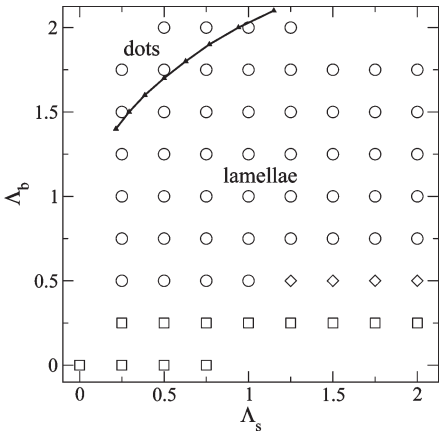

Figure 8. Equilibrium and metastability for the dot morphology. The solid line ($\Delta F = 0$) is the phase boundary between dots (above) and lamellae (below). As in Figure 3, the symbols indicate the morphology that spontaneously forms in simulations: dots (○), lamellae (□), or a hybrid morphology that includes both (◇).

the period resulting from the box width L_y. The deformation of the dots upon varying d_y is shown in Figure 7.[22] Upon compression, the pairs of dots remain perpendicular to the stripes until $d_y/L_0 \simeq 6/7 = 0.85$, where the number of pairs along a stripe shifts from seven to six. Upon stretching, pairs of dots are increasingly tilted until the structure breaks for $d_y/L_0 \simeq 10/7 = 1.43$. Both trends are reminiscent of a lamellar morphology, whose domains remain straight and parallel upon compression, while they buckle and undulate under tension.[13] This is in line with the observation that the upper part of the dot structure consists of lamellae-like domains (see Figure 2).

Using integration along the external field path, $\Delta F = F_{\mathrm{dot}} - F_{\mathrm{lam}}$ was determined for several box widths L_y. The free energy of lamellae being independent of L_y, one obtains the free energy of dots as a function of d_y, plus a constant. While the statistical uncertainty prevents us from obtaining a precise estimate of the natural period D_y, the data shown in Figure 7 suggest that D_y is close to $8/7L_0$. Furthermore, the change of ΔF when L_y varies in the range $7.5L_0-8.5L_0$ is less than 10%, suggesting that finite-size effects on ΔF are small.[23] Finally, it should be noted that the dot morphology is also periodic along the x direction. We have imposed a fixed value $L_x = 4L_0$ for the box length and assumed the associated finite-size effects are small in this case, too.

Metastability of the Dot Morphology. By computing ΔF in the $\Lambda_s-\Lambda_b$ plane, one can trace the equilibrium coexistence line between lamellae and dots (Figure 8). The dots have the lowest free energy only when the stripes and the background have respectively weak and strong affinities, whereas the lamellae is the equilibrium morphology in most of the parameter space explored. On the other hand, as shown above in Figure 3, simulations with intermediate and strong Λ_b mainly yield dots. It is thus apparent that a large portion of the parameter space is dominated by metastable dots. Note that the finite-size effects are not responsible for the observed metastability: for a given simulation box, dots spontaneously form although their free energy is higher than that of lamellae.

A rationale for the appearance of metastable dots is suggested by examining the initial stage of the self-assembly process. After starting a simulation from random initial positions and configurations of the chains, the stripes and background area are quickly covered by a layer of their preferred blocks,[24] a process also observed in previous simulations with complete patterns.[14] The subsequent formation of dots leaves this initial layer largely unaltered. In contrast, formation of lamellae requires that the layer be partially removed, particularly when the two B domains above the background are disjoint and leave an A domain in direct contact with the repulsive background. If unable to overcome this large free energy barrier, the system adopts the metastable, but kinetically favored, dot morphology. The barrier height and the final morphology depend on the background affinity. At high Λ_b, the barrier cannot be overcome within the simulation "time" and MC moves considered here, and dots are obtained. At intermediate Λ_b, dots first appear, before giving way to lamellae.

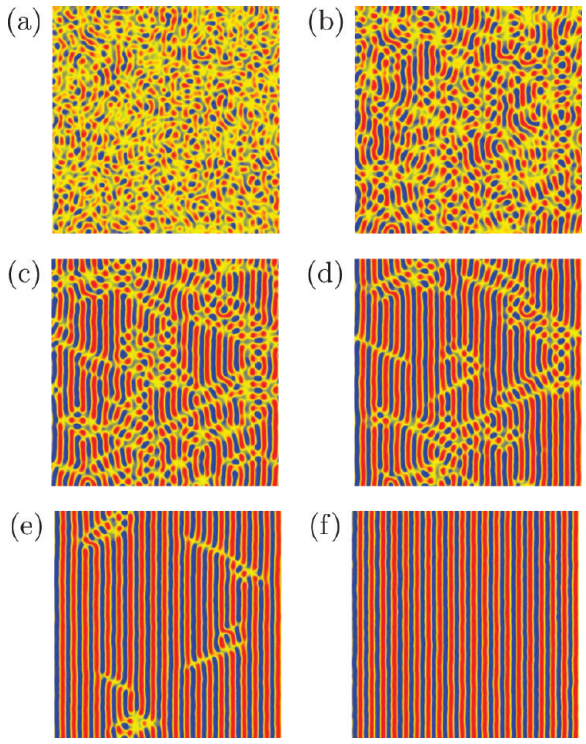

Figure 9. Different stages of the self-assembly process. Here, $L_P/L_0 = 2$, $W/L_0 = 0.5$, $\Lambda_b = 0.25$, and $\Lambda_s = 1$. Color maps (a) to (f) are taken after 200, 400, 1200, 2800, and 5200 MC steps, respectively. The box size is $20L_0$.

The transient formation of dots is illustrated in Figure 9 for a large system ($L_x = L_y = 20L_0$). For the pattern parameters considered, the final morphology consists of defect-free vertical lamellae. However, at the beginning of the simulation, after the appearance of small A and B domains, one observes alongside the growing lamellae some regions of dots that emerge simultaneously, which again suggests that the formation of dots is kinetically favored. At a later stage, the dot regions gradually shrink, leaving only lines of defects that eventually disappear. Those observations were made in MC simulations with global moves. Simulations with local moves yield a slower equilibration but otherwise give qualitatively similar results. Note that chain dynamics in real systems are further hampered by entanglements, which are not considered in this work.[25] In the presence of entanglements, overcoming the free energy barriers is even more difficult, and we therefore expect the formation of metastable dots to also arise in experimental systems. Note that the self-assembly process simulated here corresponds to a quench followed by thermal annealing. If, on the other hand, microphase separation occurs under rapid evaporation of solvent, the self-assembly should

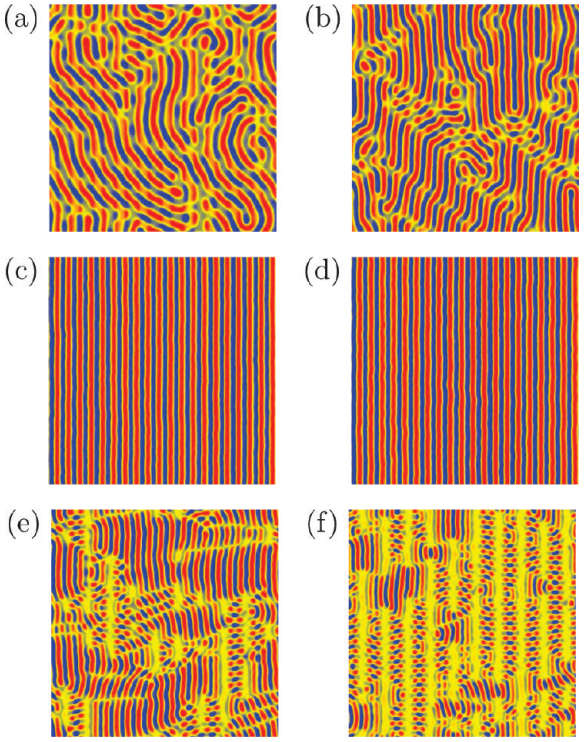

Figure 10. Effect of pattern commensurability. From color maps (a) to (f), the pattern period is L_P/L_0 = 1.6, 1.8, 2, 2.2, 2.3, and 2.5. In each case, the area shown has dimensions $10L_P \times 10L_P$.

involve an ordering front which propagates from the top of the film, where solvent concentration is the lowest, to the substrate.[15,16]

C. Effect of Pattern Commensurability. The previous sections focused on the influence of the pattern parameters W, Λ_b, and Λ_s, while keeping the pattern period constant at $L_P = 2L_0$. We now briefly examine the effects of pattern incommensurability with L_0. We fix $W = 0.25L_0$, $\Lambda_b = 0.25$, and $\Lambda_s = 1$, a set of conditions that yields interpolated vertical lamellae for $L_P = 2L_0$. The commensurability ratio $\alpha = L_P/L_0$ was varied from 1.5 to 2.5 in 0.1 increments. For each case, five distinct simulations were run in a box large enough to avoid finite size effects ($L_x = L_y = 10L_P$). Simulations were run for up to 10^5 MC steps and stopped when a perfectly ordered morphology was obtained or when the morphology exhibited little or no change over the course of the last 10^4 MC steps. As explained below, some of the final morphologies do not correspond to equilibrium but to highly metastable states that nonetheless could be relevant in experiments. Note that for the five realizations with commensurate pattern ($\alpha = 2$) the largest "time" needed to reach defect-free lamellae is 6000 MC steps; the longest simulations thus correspond to an "annealing time" that is more than 10 times larger. Some representative morphologies obtained on noncommensurate patterns are shown in Figure 10. To better characterize the morphologies, we have computed the distribution of local orientation $P(\theta)$, where θ is the angle between the stripe direction (y-axis) and the interfaces between domains. The distributions shown in Figure 11 result from an average over all realizations.

Defect-free interpolated lamellae are obtained for α = 1.9, 2, 2.1, and 2.2. For the pattern considered here, the interpolation process is rather robust vis-a-vis changes of L_P. Note that the distribution $P(\theta)$ includes angles slightly different from 0 because the lamellae interface exhibits some line edge roughness. The roughness is slightly more

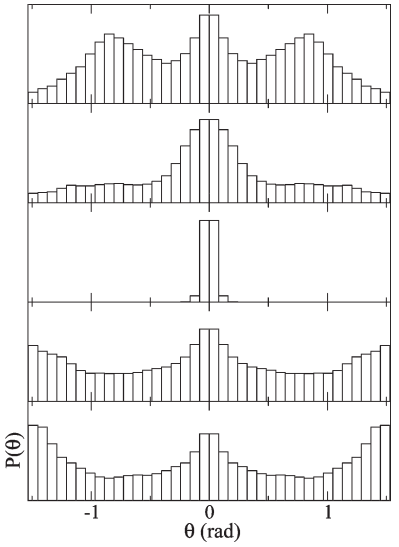

Figure 11. Local orientation of domains in morphologies obtained with varying pattern commensurability $\alpha = L_P/L_0$. From top to bottom, α = 1.6, 1.8, 2, 2.3, and 2.5. The distributions have been symmetrized.

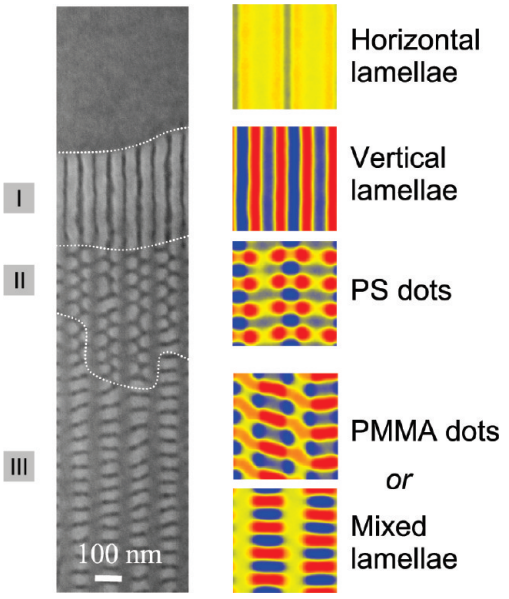

Figure 12. Comparison between experiments and simulations. (left) SEM micrograph showing four distinct morphologies. PS-rich domains appear in light gray. (right) Color maps of simulations. PS-rich domains appear in red and PMMA-rich domains in blue. See Figure 2 for details about the legend.

pronounced for α = 2.2 than for α = 2, as can be expected, given that stretching the lamellae leads to undulations of domains (in the bulk or sufficiently thick film[13,17]). The morphologies obtained for α = 1.5−1.8 are locally lamellar, but without global alignment of domains. They also differ from the fingerprint morphology seen on nonpatterned substrates, for which all orientations are equally probable. As shown in Figure 11, the distribution $P(\theta)$ is not uniform but exhibits a maximum around $\theta = 0$ that reveals the influence of the pattern. For $\alpha \leqslant 1.6$, there are two additional maxima which indicate the most favorable orientation of the domains when not aligned with the stripes. As α increases to 1.7, those secondary minima shrink and eventually disappear.

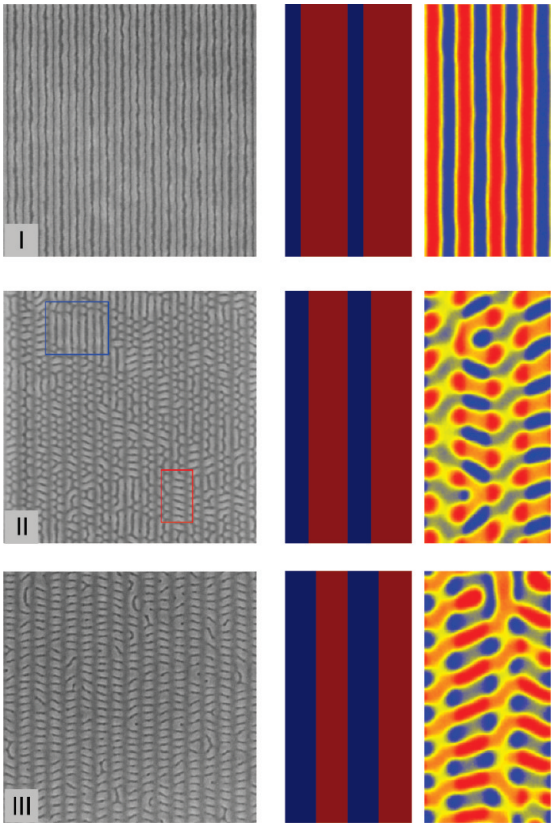

Figure 13. Effect of stripe width W: morphologies observed in experiments and tentative interpretation. (left) SEM micrographs obtained for $W/L_0 = 0.57$, 0.79, and 1.08, from top to bottom. Rectangles in micrograph II highlight regions with distinct morphologies. (right) Morphologies seen in simulations. From top to bottom, the stripe width is $W/L_0 = 0.5$,0.75, and 1; the background affinity is $\Lambda_b = 0.3$, 0.45, and 0.45. The stripe affinity is fixed at $\Lambda_s = 1$. The pattern is shown schematically on the left of the simulated color map.

For commensurability ratio $\alpha \geqslant 2.3$, we observe hybrid structures. Specifically, the case $\alpha = 2.3$ yields roughly aligned lamellae that coexist with dotlike regions. The corresponding $P(\theta)$ is bimodal with one peak at $\theta = 0$ and peaks at $\theta = \pm\pi/2$ that come from the dots. Although the rate of change is slow, lamellar regions grow at the expense of dots and defects disappear, which suggests that the equilibrium state is lamellar. Finally, the morphology seen at $\alpha = 2.5$ is distinctly different: small islands of lamellae interspersed in a sea of dots. The growth rate of lamellae is very small, which precludes a definite conclusion on the final morphology.

D. Comparison between Simulations and Experiments. The morphologies observed in experiments are illustrated in Figure 12. The micrograph obtained by SEM comprises four regions that differ only by the properties of the pattern. In addition to the structureless morphology, which presumably corresponds to horizontal lamellae, three other morphologies labeled I, II, and III are observed. To provide a tentative interpretation of these observations, we go back to Figure 2. When probing only the vicinity of the top surface ($d/L_z = 1/8$), horizontal lamellae appear as homogeneous while the vertical lamellae, dots, and checkerboard all exhibit lamellae-like domains. Only the mixed lamellae exhibit a distinctive pattern. Whereas SEM is usually assumed to probe mainly the top surface of the film, we cannot reconcile our simulation results and experimental observations under this assumption. In the following, we assume that the depth probed by the SEM is comparable to the film thickness (actually, half L_z at the minimum). With this assumption, the interpretation of micrographs becomes straightforward: morphology I corresponds to vertical lamellae, with significant asymmetry. The array of small PS domains seen in morphology II is reminiscent of the PS dots (D_{PS}). Finally, morphology III is compatible with either mixed lamellae or PMMA dots (D_{PMMA}): both structures exhibit an array of PS-rich "stitches" inserted between stripes.

To go beyond a qualitative identification of morphologies, we turn to Figure 13, which shows the self-assembled copolymers on patterns with increasingly wide stripes ($W/L_0 = 0.57$, 0.79, and 1.08). The morphologies I, II, and III are found again, this time on very large areas. In simulations, keeping Λ_b and Λ_s fixed while changing only W (with $W/L_0 = 0.5$, 0.75, and 1) does not yield three distinct morphologies compatible with those observations. To induce the first transition—from lamellae at $W/L_0 = 0.5$ to dots at $W/L_0 = 0.75$—it appears necessary to slightly increase the background affinity, for instance, from $\Lambda_b = 0.3$ to 0.45.[26] Keeping $\Lambda_b = 0.45$, the second transition—from PS dots to PMMA dots—is seen upon increasing W/L_0 from 0.75 to 1. In all cases, the stripe affinity remains fixed to $\Lambda_s = 1$ but could be chosen in a rather large window around this value.

Note that micrograph II of Figure 13 includes regions that are not dots, but rather islands of lamellae. Such "coexistence" of lamellae and dots was observed frequently in simulations. It suggests that the experimental system is not fully equilibrated, and it is tempting to speculate that the dots are metastable. Another possible explanation is that the nondot regions are induced by local variations of the pattern properties. However, inhomogeneities might then be expected in micrograph I and III as well, which is not the case.

The above interpretation has several implications. First, morphology III corresponds to PMMA dots rather than mixed lamellae. The latter is rather uncommon in the parameter space explored and arises for low Λ_b, whereas the dot morphology generally implies intermediate or high Λ_s. Second, whereas in experiments, the stripe width was varied on purpose, it is plausible that the background affinity was also changed in this process. Finally, vertical lamellae seen in experiments exhibit a visible asymmetry in the width of the PMMA domains. In simulations, such asymmetry is more pronounced for rather strong background affinities and large stripes. For the parameters considered in Figure 13, the asymmetry, if at all, is barely visible.

IV. Conclusion

Monte Carlo simulations of a coarse-grain model were applied to characterize the self-assembly of a symmetric block copolymer on an incomplete pattern. The method is sufficiently efficient to treat three-dimensional systems—a necessary requirement in the presence of patterned substrates—and to permit exploration of the parameter space by enabling simulations of hundreds of cases. Our conclusions can be summarized as follows: (i) The incomplete pattern yields several nonbulk morphologies that occupy a large portion of the parameter space. (ii) Free energy calculations show that the system can remain trapped in a metastable morphology (here dots). (iii) The most important condition to obtain interpolated lamellae is a background with low affinity. Given the uncertainty in the experimental process, we have proposed a tentative interpretation of experimental data rather than a definite assessment of our predictions.

As in previous simulation work,[14] we observed that the first stage of self-assembly is the formation of a layer that replicates the substrate pattern. This process might be beneficial when the desired self-assembled structure is a three-dimensional replicate of the pattern, as is the case for the nonregular features required in

the fabrication of integrated circuits. Indeed, the order induced near the substrate can subsequently propagate upward in the entire film. Such an ordering mechanism is not as favorable for the case of incomplete patterns, since the formation of the initial layer might lock the system in a metastable morphology and hinder the interpolated morphology. As a consequence, an optimal choice of the pattern properties should ensure not only that the desired structure corresponds to the equilibrium morphology but also that its formation be kinetically favored.

Acknowledgment. This work was supported by the National Science Foundation (NSF) through the University of Wisconsin Nanoscale Science and Engineering Center (NSEC), by the Semiconductor Research Corporation (SRC), and by the National Institute for Nano-Engineering (NINE) at Sandia National Laboratories. J.J.d.P. is grateful for a Marie Curie Fellowship from the European Community.

References and Notes

(1) Peters, R. D.; Yang, X. M.; Nealey, P. F. *Macromolecules* **2002**, *35*, 1822.
(2) Yang, X. M.; Peters, R. D.; Nealey, P. F.; Solak, F.; Harun, H.; Cerrina *Macromolecules* **2000**, *33*, 9575.
(3) Daoulas, K. C.; Muller, M.; Stoykovich, M. P.; Park, S. M.; Papakonstantopoulos, Y. J.; de Pablo, J. J.; Nealey, P. F.; Solak, H. H. *Phys. Rev. Lett.* **2006**, *96*, 036104.
(4) Park, S.-M.; Craig, G. S. W.; La, Y.-H.; Solak, H. H.; Nealey, P. F. *Macromolecules* **2007**, *40*, 5084.
(5) Ruiz, R.; Kang, H.; Detcheverry, F. A.; Dobisz, E.; Kercher, D. S.; Albrecht, T. R.; de Pablo, J. J.; Nealey, P. F. *Science* **2008**, *321*, 936.
(6) Cheng, J. Y.; Rettner, C. T.; Sanders, D. P.; Kim, H.-C.; Hinsberg, W. D. *Adv. Mater.* **2008**, *20*, 3155.
(7) Tada, Y.; Akasaka, S.; Yoshida, H.; Hasegawa, H.; Dobisz, E.; Kercher, D.; Takenaka, M. *Macromolecules* **2008**, *41*, 9267.
(8) Fredrickson, G. H. *The Equilibrium Theory of Inhomogeneous Polymers*; Clarendon Press: Oxford, 2006.
(9) Detcheverry, F. A.; Kang, H.; Daoulas, K. C.; Müller, M.; Nealey, P. F.; de Pablo, J. J. *Macromolecules* **2008**, *41*, 4989.
(10) Daoulas, K. C.; Muller, M.; Stoykovich, M. P.; Papakonstantopoulos, Y. J.; De Pablo, J. J.; Nealey, P. F.; Park, S. M.; Solak, H. H. *J. Polym. Sci., Part B: Polym. Phys.* **2006**, *44*, 2589.
(11) Müller, M.; Daoulas, K. C. *J. Chem. Phys.* **2008**, *128*, 024903.
(12) Detcheverry, F. A.; Pike, D. Q.; Nealey, P. F.; Müller, M.; de Pablo, J. J. *Phys. Rev. Lett.* **2009**, *102*, 197801.
(13) Wang, Z. *J. Chem. Phys.* **1994**, *100*, 2298.
(14) Edwards, E. W.; Stoykovich, M. P.; Muller, M.; Solak, H. H.; De Pablo, J. J.; Nealey, P. F. *J. Polym. Sci., Part B: Polym. Phys.* **2005**, *43*, 3444.
(15) Lin, Z.; Kim, D.; Wu, X.; Boosahda, L.; Stone, D.; LaRose, L.; Russell, T. *Adv. Mater.* **2002**, *14*, 1373.
(16) Buxton, G. A.; Clarke, N. *Europhys. Lett.* **2007**, *78*, 56006.
(17) Kim, S. O.; Kim, B. H.; Kim, K.; Koo, C. M.; Stoykovich, M. P.; Nealey, P. F.; Solak, H. H. *Macromolecules* **2006**, *39*, 5466.
(18) Pike, D. Q.; Detcheverry, F. A.; Müller, M.; de Pablo, J. J. *J. Chem. Phys.* **2009**, *131*, 084903.
(19) For a detailed discussion of the choice of κN, see ref 18.
(20) Affinities above $\Lambda N = 2$ induce a significant increase in the total polymer density in the vicinity of the wall; this is an artifact of the high compressibility of the system.
(21) At each Monte Carlo step, a bead is moved on average once, with the convention that global moves affecting the whole chain (translation, reptation, and swapping of the two blocks) displace N beads.
(22) The configuration obtained for $L_y = 8L_0$ was used as an initial condition for the simulation with different box size: the bead positions were rescaled to the new box size, and the number of polymer chains adjusted to keep the bead density constant.
(23) Such an analysis was conducted for the single point $\Lambda_s = \Lambda_b = 1$. However, among all simulations run with other parameters, none led to a different number of dots, which suggests that D_y does not change drastically over the parameter region explored.
(24) This applies when using Monte Carlo moves that are global or local.
(25) Because of the soft interaction potential between beads, chains can cross each other in our simulations.
(26) With this choice of pattern affinities, the transition from lamellae to dots is clearly visible. Five realizations were run for each combination of parameters. For $\Lambda_b = 0.3$ and $W/L_0 = 0.5$, all simulations converge to lamellae. For $\Lambda_b = 0.45$ and $W/L_0 = 0.75$, all simulations converge to dots.